

Evidence of a metal-rich surface for the asteroid (16) Psyche from interferometric observations in the thermal infrared [☆]

Alexis Matter^{a,1,*}, Marco Delbo^b, Benoît Carry^c, Sebastiano Ligori^d

^a*Max Planck institut für Radioastronomie, auf dem Hügel, 69, 53121, Bonn, Germany.*

^b*UNS-CNRS-Observatoire de la Côte d'Azur, Laboratoire Lagrange, BP 4229 06304 Nice
cedex 04, France.*

^c*IMCCE, Observatoire de Paris, UPMC, CNRS, 77 Av. Denfert Rochereau, 75014
Paris, France.*

^d*INAF-Osservatorio Astronomico di Torino, Strada Osservatorio 20, 10025 Pino
Torinese, Torino, Italy.*

Number of pages: 45

Number of tables: 2

Number of figures: 5

[☆]Based on observations collected at the European Southern Observatory (ESO), Chile:
ESO Program ID 386.C-0928

*Corresponding author.

Email addresses: alexis.matter@obs.ujf-grenoble.fr (Alexis Matter),
delbo@oca.eu (Marco Delbo), bcarry@imcce.fr (Benoît Carry), ligori@oato.inaf.it
(Sebastiano Ligori)

¹Present address: Institut de planétologie et d'astrophysique de Grenoble, 414, rue de
la Piscine, 38400 Saint Martin d'Hères, France.

Proposed running head: Infrared interferometry of the
asteroid (16) Psyche.

Editorial correspondence and proofs should be directed
to:

Alexis Matter

Institut de Planétologie et d'Astrophysique de Grenoble,
414 rue de la Piscine, 38400 Saint Martin d'Hères,
France.

email: alexis.matter@obs.ujf-grenoble.fr;

Tel: +33 4 76 63 58 30

Fax: +33 4 76 44 88 21

Abstract

1 We describe the first determination of thermal properties and size of the
2 M-type asteroid (16) Psyche from interferometric observations obtained with
3 the Mid-Infrared Interferometric Instrument (MIDI) of the Very Large Tele-
4 scope Interferometer. We used a thermophysical model to interpret our in-
5 terferometric data. Our analysis shows that Psyche has a low macroscopic
6 surface roughness. Using a convex 3-D shape model obtained by Kaasalainen
7 et al. (2002, *Icarus* 159, 369–395), we derived a volume-equivalent diameter
8 for (16) Psyche of 247 ± 25 km or 238 ± 24 km, depending on the pos-
9 sible values of surface roughness. Our corresponding thermal inertia esti-
10 mates are 133 or $114 J m^{-2} s^{-0.5} K^{-1}$, with a total uncertainty estimated at
11 $40 J m^{-2} s^{-0.5} K^{-1}$. They are among the highest thermal inertia values ever
12 measured for an asteroid of this size. We consider this as a new evidence of
13 a metal-rich surface for the asteroid (16) Psyche.

14 Keywords

15 Asteroids; Asteroids surfaces; Infrared observations; Data reduction tech-
16 niques.

17 **1. Introduction**

18 Asteroids classified in the X-complex (in the taxonomies by [Bus and Binzel](#)
19 [2002](#); [DeMeo et al. 2009](#)) are characterized by a visible and near-infrared re-
20 flectance spectrum that is essentially featureless and moderately red in the
21 [0.3-2.5] micron region. The spectroscopic X-complex can be split into three
22 taxonomic classes, E, M and P, according to albedo ([Tholen 1984](#)). M-type
23 asteroids are distinguished by exhibiting moderate geometric visible albedos
24 of about 0.1 to 0.3. Due to the lack of absorption features in the spectrum
25 of M-type asteroids, the nature of these objects remains uncertain. Histor-
26 ically, M-class asteroids were assumed to be the exposed metallic core of
27 differentiated parent bodies that were catastrophically disrupted, and thus
28 the source of iron meteorites ([Bell et al. 1989](#); [Cloutis et al. 1990](#)). While the
29 parent bodies of meteorites are usually assumed to have formed in the main
30 belt, [Bottke et al. \(2006\)](#) showed that the iron-meteorite parent bodies most
31 probably formed in the terrestrial planet region. Some of the metallic ob-
32 jects currently located in the main-belt may thus not be not indigenous and
33 possibly remnants of the precursor material that formed the terrestrial plan-
34 ets including the Earth. Therefore, those objects play a fundamental role in
35 the investigations of the solar system formation theories. Radar observa-
36 tions provided strong evidences for the metallic composition of a least some
37 M-type asteroids. Very high radar albedos have been measured for various as-
38 teroids of this class, consistent with high concentration of metal ([Ostro et al.](#)
39 [1985](#); [Shepard et al. 2008](#)). Moreover, the average density of two multiple
40 M-type asteroids, 3.35 g.cm^{-3} ([Descamps et al. 2008](#)) for (22) Kalliope and
41 3.6 g.cm^{-3} ([Descamps et al. 2011](#)) for (216) Kleopatra, appeared to be sig-

42 nificantly larger than the density of C-type or S-type asteroids (Carry 2012).
43 This is a strong evidence of difference in internal composition between M
44 and C-type asteroids. However, recent visible and near-infrared spectro-
45 scopic surveys on about 20 M-type asteroids, including those exhibiting high
46 radar albedos, detected subtle spectral absorption features on most of them
47 (Hardersen et al. 2005; Fornasier et al. 2010). The most common one be-
48 ing the 0.9 μm absorption feature, attributed to orthopyroxene, and thus
49 indicating the presence of silicate on their surface. From a survey of the
50 3 μm spectrum of about 30 M-type asteroids, Rivkin et al. (1995, 2000) also
51 found hydration features on a tens of them. On the basis of these obser-
52 vations, they suggested that the original “M” class should be divided into
53 “M” asteroids that lack hydration features such as (16) Psyche and (216)
54 Kleopatra, and “W” asteroids that are hydrated such as (21) Lutetia. All of
55 that confirms that most of the objects defined by the Tholen M-class have
56 not a pure metallic surface composition but contain other species including
57 silicate minerals. Therefore, better compositional constraints for the spec-
58 trally featureless bodies like M-type asteroids are essential in order to better
59 understand and constrain the thermal, collisional, and migration history of
60 Main-Belt Asteroids (MBAs). This includes the detection of additional ab-
61 sorption features in their reflectance spectra and the determination of their
62 surface properties including surface roughness and in particular thermal in-
63 ertia.

64 Thermal inertia (Γ) is a measure of the resistance of a material to tem-
65 perature change. It is defined by $\Gamma = \sqrt{\rho\kappa c}$, where κ is the thermal con-
66 ductivity, ρ the material density and c the specific heat. The value of

67 thermal inertia thus depends on the material properties (see [Mueller 2007](#),
68 and references therein for a table of the value of the thermal inertia of
69 some typical materials). On one hand, it primarily informs us about the
70 nature of the surface regolith: a soil with a very low value of Γ , for in-
71 stance in the range between 20 and 50 $J m^{-2} s^{-0.5} K^{-1}$, is covered with
72 fine dust like on Ceres ([Mueller and Lagerros 1998](#)); an intermediate value
73 (150-700 $J m^{-2} s^{-0.5} K^{-1}$) indicates a coarser, mm- to cm-sized, regolith
74 as observed on (433) Eros ([Veveřka et al. 2001a,b](#)) and (25143) Itokawa
75 ([Yano et al. 2006](#)), respectively; solid rock with very little porosity is known
76 to have thermal inertia values of more than 2500 $J m^{-2} s^{-0.5} K^{-1}$ ([Jakosky](#)
77 [1986](#)). On the other hand, thermal inertia can represent a proxy for the
78 surface composition, especially due to its dependency on thermal conductiv-
79 ity and specific heat. This is particularly important in the context of the
80 M-type asteroids study since metal is an excellent thermal conductor, po-
81 tentially leading to an enhanced thermal inertia. The study of [Opeil et al.](#)
82 ([2010](#)) showed that thermal conductivity is significantly higher for iron me-
83 teorites than for non-metallic ones. This motivates our work of determining
84 thermal inertia on M-type asteroids such as (16) Psyche to assess the change
85 in thermal inertia for asteroids of different composition but having a simi-
86 lar size, knowing that the presence and thickness of the surface regolith is
87 generally assumed to depend on the asteroid’s size (see, e.g., [Bottke et al.](#)
88 [2005](#)).

89 The asteroid (16) Psyche is the largest known M-type asteroid, with an
90 IRAS diameter of 253 ± 4 km ([Tedesco et al. 2002](#)). Nevertheless, many size
91 estimates have been reported during the last decade. [Cellino et al. \(2003\)](#) de-

92 rived an area equivalent diameter of 288 ± 43 km based on speckle interferome-
93 try; [Lupishko \(2006\)](#) derived a diameter of 213 km based on considerations on
94 its polarimetric albedo; from adaptive-optics imaging, [Drummond and Christou](#)
95 [\(2008\)](#) derived a volume equivalent diameter of 262 ± 6 km; [Shepard et al.](#)
96 [\(2008\)](#) derived a volume equivalent diameter of 186 ± 30 km based on radar
97 imaging; from the analysis of medium infrared data from the AKARI satellite
98 by means of the Standard Thermal Model ([Lebofsky et al. 1986](#)), [Usui et al.](#)
99 [\(2011\)](#) derived a diameter of 207 ± 3 km; finally, [Durech et al. \(2011\)](#) derived
100 a volume equivalent diameter of 211 ± 21 km by combining a shape model de-
101 rived by lightcurve inversion with occultation observations of (16) Psyche. In
102 any case, Psyche appears to be significantly larger than the 30-90 km diam-
103 eter expected for the metallic core of a differentiated asteroid ([Rivkin et al.](#)
104 [2000](#)), questioning a purely metallic nature for this asteroid. All those size
105 measurements led to significant differences between the average bulk den-
106 sity estimations reported in the literature. They range from $1.8 \pm 0.6 \text{ g.cm}^{-3}$
107 ([Viateau 2000](#)) to $3.3 \pm 0.7 \text{ g.cm}^{-3}$ ([Drummond and Christou 2006](#)) and even
108 $6.58 \pm 0.58 \text{ g.cm}^{-3}$ ([Kuzmanoski and Kovačević 2002](#)), value which is more
109 in agreement with a metallic composition and a very low macroporosity.
110 Nevertheless, by combining all the independent size and mass estimates, an
111 average density of $3.36 \pm 1.16 \text{ g.cm}^{-3}$ was found ([Carry 2012](#)). This is com-
112 parable to the density estimates reported for other M-type asteroids like
113 (22) Kalliope ([Descamps et al. 2008](#)) and (216) Kleopatra ([Descamps et al.](#)
114 [2011](#)). In addition, ([Shepard et al. 2010](#)) measured a high radar albedo of
115 0.42, which is indicative of a metal-rich surface. However, the detection of
116 a $0.9 \mu\text{m}$ absorption feature suggested the presence of silicates on its sur-

117 face ([Hardersen et al. 2005](#)). In this context, [Hardersen et al. \(2005\)](#) and
118 [Shepard et al. \(2010\)](#) suggested that (16) Psyche may be a collisional aggre-
119 gate of several objects, including partial or intact metallic cores that have
120 retained a portion of their silicate-rich.

121 To put tighter constraints on the nature of (16) Psyche, we used mid-
122 infrared interferometry to determine the thermal properties of this asteroid,
123 and refine its size measurements. Interferometry basically provides direct
124 measurements of the angular extension of the asteroid along different direc-
125 tions ([Delbo et al. 2009](#)). Interferometric asteroid observations in the ther-
126 mal infrared, where the measured flux is dominated by the body’s thermal
127 emission, are sensitive to the surface temperature spatial distribution in dif-
128 ferent directions on the plane of the sky. The typical spatial resolution is
129 about 0.06 "in the case of our Psyche observations. As the surface tem-
130 perature distribution of atmosphereless bodies is affected by thermal inertia
131 and surface roughness, interferometric thermal infrared data can be used to
132 constrain these parameters. In particular, thermal infrared interferometry
133 can help to remove the degeneracy existing between the effect of the ther-
134 mal inertia and surface roughness in one single epoch (see Figs. 7 and 8 in
135 [Matter et al. 2011](#)), providing that we have several interferometric measure-
136 ments with different projected baseline lengths and orientations, during the
137 asteroid rotation. Thermal properties (thermal inertia and surface rough-
138 ness) can thus be better constrained by thermal infrared interferometry in
139 combination with the classical disk-integrated radiometry. In this context, we
140 obtained interferometric data on (16) Psyche using the MIDI instrument com-
141 bining two of the Auxiliary Telescopes (ATs) of the VLTI. As in [Matter et al.](#)

142 (2011), a thermophysical model (TPM), taking into account the asteroid's
143 orbit, spin, shape, and heat diffusion into the subsurface, was used for the
144 analysis of the whole data set.

145 In section 2 we report the observations and the data reduction process
146 that we adopted; in section 3 we briefly remind the principles of the thermo-
147 physical model used for the interpretation of MIDI data, and we detail the
148 shape models that we used; in section 4, we present our results, followed by
149 a discussion in section 5.

150 2. Observations and data reduction

151 2.1. Observations

152 The observations of (16) Psyche were carried out in visitor mode, on
153 2010 December 30. Two ATs were used in the E0-G0 configuration (base-
154 line $B = 16$ m). Sky quality was relatively good and stable during those
155 nights (see Table 1). We adopted the typical observing sequence of MIDI,
156 which is extensively described by [Leinert et al. \(2004\)](#). For each of the five
157 observing epochs of (16) Psyche (indicated in Table 1), we obtained one mea-
158 surement of the total flux and of the interferometric visibility, both dispersed
159 over the N-band, from 8 to 13 μm . We used the HIGH-SENS mode, where
160 the total flux of the source is measured right after the fringe tracking and
161 not simultaneously. To disperse the fringes, we used the prism of MIDI,
162 which gives a spectral resolution of $\frac{\lambda}{\Delta\lambda} \approx 30$ at $\lambda = 10 \mu\text{m}$. Our observa-
163 tions also included a mid-infrared photometric and interferometric calibrator

164 HD 29139, taken from the ESO database using the Calvin tool ², which is
165 the calibrator selector for the VLTI instruments (MIDI and AMBER). We
166 remind that interferometric calibrators are stars that have small and known
167 angular diameter, so that their visibility is close to unity at all wavelengths.
168 This calibrator was chosen to have a minimum angular separation with the
169 source ($\approx 3^\circ$) and a similar airmass, as shown in Table 1. This Table also
170 summarizes the log of observations, with the corresponding interferometric
171 parameters.

172

173 [Table 1 about here.]

174 2.2. Data reduction

175 Extraction and calibration of the flux and visibility measurements of (16)
176 Psyche were performed using the data reduction software package EWS (Ex-
177 pert WorkStation). This publicly available³ software performs a coherent
178 analysis of dispersed fringes to estimate the complex visibility of the source.
179 The method and the different processing steps are described in Jaffe (2004).
180 The calibration of the fluxes and visibilities was performed using the closest
181 calibrator observation in time. Calibrated fluxes of (16) Psyche were ob-
182 tained by multiplying the ratio target/calibration star raw counts, measured
183 by MIDI at each wavelength, by the absolute flux of the calibrator. The
184 absolutely calibrated infrared spectrum of our calibrator was taken from a

²Available at <http://www.eso.org/observing/etc/>

³Software package is available at <http://home.strw.leidenuniv.nl/~jaffe/ews/index.html>

185 database created by R. van Boekel, which is initially base on infrared tem-
186 plates created by [Cohen et al. \(1999\)](#). More details can be found in [Verhoelst](#)
187 [\(2005\)](#). The instrumental visibilities of (16) Psyche correspond to the ratio
188 of the source raw correlated flux and the source raw photometric flux. The
189 calibrated visibilities of (16) Psyche were then derived by dividing the in-
190 strumental visibility by the visibility measured on the calibrator for each ob-
191 serving epoch. We refer the reader to [Delbo et al. \(2009\)](#) for a more detailed
192 description of the data reduction and calibration of MIDI interferometric
193 data.

194 The five calibrated flux and visibility measurements of (16) Psyche are shown
195 in Fig 1. The error bars represent the statistical noise contribution affecting
196 the correlated and total flux measurements. It is estimated by splitting a
197 complete exposure, consisting of several thousand of frames, into five equal
198 parts and deriving the variance of these sub-observations. In the error bud-
199 get, we neglected the error due to the variability of the interferometer transfer
200 function during the night. However this is not a problem since, by computing
201 the rms of the transfer function, i.e., the instrumental visibility provided by
202 the calibrator observations, we found a very good stability all over the night.

203 *2.3. Observational results*

204 [Figure 1 about here.]

205 At each observing epoch, the corresponding visibility is pretty low ($\approx 0.1 -$
206 0.4), thus indicating that the object is very well resolved by MIDI. More-
207 over we can notice a significant decrease of the visibility level between the
208 first and second epochs, which are separated by 2h30, and then only slight

209 changes in the visibility shape and level for the next epochs. This behaviour
210 can be explained by the increase of the length of the projected baseline
211 during the observing night (see Table 1), combined to the evolution of the
212 projected baseline orientation and the asteroid rotation. For instance, the
213 difference between the first and last visibility measurements is mainly due to
214 the increase of the projected baseline length since our observations covered
215 a complete rotation of the asteroid (≈ 4.2 h), without a significant evolu-
216 tion of the baseline orientation. This is illustrated in Figure 2, where we
217 represented the expected orientation of (16) Psyche at the time of the VLTI
218 observations. Here, we considered the two existing pole solutions derived by
219 [Kaasalainen et al. \(2002\)](#) and that we detail hereafter in Section 3.

220 [Figure 2 about here.]

221 3. Thermophysical modeling

222 The thermophysical modeling of interferometric data is extensively de-
223 scribed in [Matter et al. \(2011\)](#), and references therein), and here we briefly
224 remind its principles, along with the shape model we used for this modeling.
225 The thermal inertia and macroscopic roughness of an asteroid can be derived
226 by comparing measurements of the thermal-infrared flux and interferometric
227 visibility of the body to synthetic fluxes and visibilities generated by means
228 of a thermophysical model (TPM). A TPM uses the spin vector information
229 to orient a 3-D shape model, composed of a mesh of planar facets, at the
230 time of the observing epochs. The temperature of each facet is calculated by
231 solving the one-dimensional heat diffusion equation (where the heat diffusion

232 is between the surface and the shallow subsurface) using presets thermal in-
233ertia values. Surface roughness is modeled by adding hemispherical craters of
234variable opening angle, γ_c , and surface density, ρ_c . As for [Delbo and Tanga](#)
235(2009), thermal conduction within the craters is also modeled. Albedo, ther-
236mal inertia, surface roughness and emissivity are assumed constant over the
237asteroid’s surface. We remind that emissivity, noted hereafter ϵ , has nor-
238mally directional properties and drops at higher viewing angles, in particular
239at the limb of objects having a smooth surface (see e.g., [Jakosky et al. 1990](#)).
240However, we expect it to be a second-order effect since the limb normally con-
241tributes much less to the thermal emission than the nadir, especially if the
242object was observed under a low solar phase angle like for our observations
243of (16) Psyche. We also assumed ϵ achromatic and equal to 0.9, which is a
244typical value for silicate powders and is commonly assumed for the surface of
245asteroids ([Emery et al. 2006](#); [Mueller 2007](#)). However, regarding the possible
246metallic nature of the Psyche’s regolith, it is worth mentioning that metals
247have usually emissivities lower than 0.9 depending on their state of roughness
248and porosity. For instance, powdered iron at a temperature of 300 K and with
249a porosity similar to the lunar regolith ($\approx 50\%$), has $\epsilon \approx 0.8$ ([Sih and Barlow](#)
2502004). Assuming that the regolith of (16) Psyche is purely ferrous, we thus
251ran in parallel our TPM with $\epsilon = 0.8$. As a result, only tiny changes were
252observed in terms of size, thermal inertia and surface roughness. Moreover,
253silicate material was detected on the Psyche’s surface ([Hardersen et al. 2005](#)),
254and could increase the surface emissivity. Therefore, we finally kept $\epsilon = 0.9$
255for the thermophysical modeling of (16) Psyche.
256Following the procedure described in [Matter et al. \(2011\)](#), the best-fit value

257 of a , which is the linear mesh scale factor, for each discrete value of Γ and
 258 each roughness model can be found by minimizing a χ^2 function taking into
 259 account both the integrated flux and the interferometric visibility. Then,
 260 the location of the minimum χ^2 as a function of Γ gives the best-fit asteroid
 261 surface thermal inertia for each roughness model. Eventually, the value of a
 262 at Γ -minimum is used to determine the best-fit value of the volume equiv-
 263 alent diameter of the mesh, $D_v = 2 \left(\frac{3V}{4\pi} \right)^{\frac{1}{3}}$, where V is the volume of the mesh.

264

265 Two convex mesh were downloaded from the Database of Asteroid Mod-
 266 els from Inversion Techniques⁴ (DAMIT, see [Durech et al. 2010](#)). Both shape
 267 models are characterized by a sidereal rotation period (P), and a pole solution
 268 giving the spin axis direction, which was initially derived by [Kaasalainen et al.](#)
 269 (2002) from inversion of optical lightcurves. Note that while inversion of op-
 270 tical lightcurves reconstruct the 3D shape of an asteroid, these shapes are
 271 convex by construction and do not provide any size information. The models
 272 derived from the optical lightcurves inversion are thus scaled to unity vol-
 273 ume. Later on, the two shape models of (16) Psyche were refined and scaled
 274 by [Durech et al. \(2011\)](#) using occultation data. The associated two possible
 275 pole solutions are:

276 • solution 1: $\lambda_0=32^\circ$ $\beta_0=-7^\circ$, $P=4.195948$ h

277 • solution 2: $\lambda_0=213^\circ$ $\beta_0=0^\circ$, $P=4.195948$ h

278 where λ_0 and β_0 are the ecliptic longitude and latitude of the spin axis di-
 279 rection (J2000.0, in degree), and P is the sidereal rotation period. The

⁴ <http://astro.troja.mff.cuni.cz/projects/asteroids3D/>

280 corresponding volume-equivalent diameters, derived from occultation data,
 281 are 211 ± 21 km (solution 1) and 209 ± 29 km (solution 2). Interestingly,
 282 [Durech et al. \(2011\)](#) reported that only the first pole solution reported by
 283 [Kaasalainen et al. \(2002\)](#) was consistent with all the occultation chords.
 284 Moreover, [Hanus et al. \(2012\)](#) identified the same best pole solution from
 285 comparison of adaptive-optics images and the shape models. They derived
 286 an equivalent diameter of 209 ± 9 km. In parallel, [Kaasalainen et al. \(2002\)](#)
 287 suggested the existence of albedo variegations over the surface of (16) Psy-
 288 che. They detected the signature of a bright spot of moderate size, which is
 289 about 30% brighter than the rest of the surface. However, albedo variega-
 290 tions have little effect on the thermal emission. In particular, by increasing
 291 the geometric visible albedo of 30%, the $10 \mu\text{m}$ flux vary by about 2%, which
 292 is within the error bars of our MIDI measurements. Therefore, the assump-
 293 tion of thermal homogeneity (thermal inertia, surface roughness) over the
 294 asteroid surface should not be affected by this bright spot.

295 Using both shape models, the TPM was run for each roughness model,
 296 and thermal inertia values of 5, 10, 25, 50, 75, 100, 125, 150, 175, 200, 300,
 297 400, 500, 750 and $1000 J m^{-2} s^{-0.5} K^{-1}$. The roughness models we used
 298 are: ‘no roughness’ ($\gamma_c = 0^\circ$, $\rho_c = 0$), ‘low roughness’ ($\gamma_c = 45^\circ$, $\rho_c = 0.5$),
 299 ‘medium roughness’ ($\gamma_c = 68^\circ$, $\rho_c = 0.75$), and ‘high roughness’ ($\gamma_c = 90^\circ$,
 300 $\rho_c = 1.0$). Then the fit procedure described in section 3 was applied to the
 301 measured fluxes and visibilities, each of them containing 47 points between
 302 8 and $13 \mu\text{m}$. The flux and visibility measurements shown in Figure 1 are
 303 the inputs of the thermophysical model.

304 In the next section we describe and discuss the results obtained from the

305 application of the TPM to the observed visibilities and fluxes of (16) Psyche.

306 4. Results

307 Fig. 3 shows our reduced χ^2 estimator as a function of Γ for the four dif-
308 ferent roughness models, in the case of the two pole solutions described above.

309

310 [Figure 3 about here.]

311 We note that a surface with a low or no macroscopic roughness and a
312 value of thermal inertia of about $130 J m^{-2} s^{-0.5} K^{-1}$ give the best fit to
313 the observations, for both pole solutions. However, it clearly appears that
314 the pole and shape solution 1 gives a better fit to our MIDI data than the
315 pole and shape solution 2, by a factor of about 5. This is in agreement with
316 the conclusions of Durech et al. (2011) and Hanus et al. (2012) who favored
317 the first pole solution. Therefore, we adopt the pole and shape solution 1 for
318 the determination of thermal properties of (16) Psyche.

319 To refine the estimation of the best-fit thermal inertia values, we ran
320 the TPM for additional values, namely, $\Gamma = 105, 110, 115, 120, 130, 135,$
321 $140, 145, 155, 165$. Then, using a polynomial interpolation, we found the
322 minima of the ‘no roughness’ and ‘low roughness’ models at $\Gamma=133$ and
323 $114 J m^{-2} s^{-0.5} K^{-1}$, respectively. The reduced χ^2 values of those two best-
324 fit models are 3.26 and 3.14, respectively. To obtain the best-fit values for D_V ,
325 we multiplied the volume-equivalent diameter of the mesh (211 km) by the
326 best-fit scale factor values we got from our fit, namely 1.17 and 1.13 for the
327 ‘no roughness’ and ‘low roughness’ models, respectively. The corresponding

328 values of D_V are 247 and 238 km, with associated p_V values of 0.12 and 0.13,
 329 respectively; for the calculation of p_V , we considered an absolute magnitude
 330 H of 5.93 according to [Pravec et al. \(2012\)](#). In parallel, we also forced the
 331 volume equivalent diameter of the mesh to its nominal value (211 km for the
 332 solution 1) in order to assess its effect on our thermal inertia determination.
 333 We thus fixed the mesh scale factor to 1, and recalculated a χ^2 value for
 334 each roughness model and thermal inertia value. It appeared that the fit to
 335 the visibility and flux measurements is significantly worse for any roughness
 336 model ($\chi_{\text{red}}^2 \geq 50$) while the best-fit values for thermal inertia are slightly
 337 lower (between 90 and 110 $J m^{-2} s^{-0.5} K^{-1}$). In [Fig. 1](#) we plot the visibility
 338 and flux of the best-fit model ('low roughness', $\Gamma = 114 J m^{-2} s^{-0.5} K^{-1}$,
 339 $D_V = 238$ km, $p_V = 0.13$), in addition to the measured fluxes and visibilities
 340 of (16) Psyche. We note that our model represents well the observed flux
 341 except for the long-wavelength edge of the N band. Indeed, for the second
 342 and fifth observing epochs, the TPM flux is greater than the measured one
 343 by roughly 10% at 13 μm . This 'offset-like' mismatch may come from an
 344 underestimation of the total flux of the source by MIDI, due to a bad es-
 345 timation and subtraction of the thermal background (and its fluctuations),
 346 which is dominant in the mid-infrared (see, e.g., [Perrin et al. 2003](#)). This
 347 is especially problematic around 13 μm where the atmospheric transmission
 348 starts to be degraded by water absorption lines. Since the MIDI correlated
 349 flux measurements are usually not very much affected by background sub-
 350 traction (see e.g., [Chesneau 2007](#)), an underestimation of the photometry
 351 would bring an increase in the visibility. However, since the fringe contrast
 352 is low, this effect is not noticeable in our visibility measurements. The fit

353 to the visibilities generally appears good and follow the same trend as the
354 measurements, confirming the good match of the shape model to the inter-
355 ferometric data.

356 In order to search for the presence of possible emission features in the
357 mid-infrared spectrum of (16) Psyche, we plotted in Figure 4 the ratio be-
358 tween the MIDI flux measurement and our best-fit TPM for each observing
359 epoch. Only the first epoch shows marginal detection of a possible emission
360 feature between 8 and 10 μm that could be associated with the Christiansen
361 peak around 9 μm . The error bars shown in Figure 4 represent the statisti-
362 cal uncertainty affecting the MIDI measurements. However, bad estimation
363 and removal of the strong thermal background over the N band and/or the
364 atmospheric ozone absorption feature around 9.6 μm can imply additional
365 uncertainties of the order of 10% on the absolute level of MIDI photometry
366 measurements (see e.g., [Chesneau 2007](#)). We thus think this most likely ap-
367 plies to the ‘absorption feature’ around 9.6 μm in the fifth epoch plot, and
368 then probably also to the ‘emission’ pattern between 8 and 10 μm in the
369 first epoch plot. As a consequence, we cannot report with confidence the
370 detection of an emission feature in the mid-infrared spectrum of (16) Psyche.

371 [Figure 4 about here.]

372 To estimate the statistical uncertainty affecting the fit parameters Γ and
373 D_V , we followed the Monte-Carlo procedure described in [Matter et al. \(2011\)](#):
374 200 normally distributed flux and visibility values per observation were gen-
375 erated at each wavelength, with average and standard deviation matching
376 the data within their respective $1\text{-}\sigma$ uncertainty; then for each set of fluxes

377 and visibilities, a new χ^2 was computed; finally we took the standard deviation of the best-fit Γ and D_V values, found for all the synthetic data set, as
 378 the 1- σ uncertainty on our best-fit value for Γ and D_V . As a result we find
 379 $\Gamma = 133 \pm 2 J m^{-2} s^{-0.5} K^{-1}$, $D_V = 247 \pm 1$ km as the best fit solution for a
 380 model without roughness; and $\Gamma = 115 \pm 2 J m^{-2} s^{-0.5} K^{-1}$, $D_V = 238 \pm 1$
 381 km as the best fit solution for a model with a low roughness. Therefore,
 382 the 1- σ statistical error from the Monte Carlo procedure is about 1% on the
 383 volume equivalent diameter and 2% on the thermal inertia. This is very low,
 384 as expected from the statistical noise affecting the MIDI measurements, and
 385 probably underestimates the true uncertainty on our thermal inertia and di-
 386 ameter estimates. Indeed, in thermophysical modeling, this uncertainty is
 387 generally dominated by the model systematics, as this was the case for the
 388 first thermophysical modeling of the interferometric data of (41) Daphne.
 389 [Matter et al. \(2011\)](#) estimated such a systematic error to be of about 7%
 390 on the diameter, taking into account only the contribution from the sur-
 391 face roughness modeling. In the case of (16) Psyche, the model systematics
 392 due to the surface roughness modeling is estimated by considering the two
 393 plausible solutions in terms of our best-fit indicator, i.e., no roughness and
 394 $\Gamma=133 J m^{-2} s^{-0.5} K^{-1}$, and low roughness and $\Gamma=114 J m^{-2} s^{-0.5} K^{-1}$.
 395 The corresponding uncertainty would thus be 9 km, i.e., 3% in relative un-
 396 certainty for D_V , and $19 J m^{-2} s^{-0.5} K^{-1}$, i.e., 15% in relative uncertainty
 397 for Γ . However, the systematic uncertainty budget probably includes ad-
 398 ditional contributions from the spin solution, the assumption of isotropic
 399 emissivity, the shape model itself and especially the albedo variegations that
 400 impact the optical lightcurves inversion process. This last point may be im-
 401

402 portant here since [Kaasalainen et al. \(2002\)](#) found evidences of a bright spot
 403 (about 30% brighter) on one side of the (16) Psyche’s surface. However, we
 404 could not properly estimate the contribution of these sources of uncertainty
 405 in the TPM. Therefore, we finally adopted a conservative error value of 10%
 406 in D_V , as generally considered in other thermophysical models (see, e.g.,
 407 [Mueller et al. 2010](#); [Marchis et al. 2012](#)). For thermal inertia, we estimated
 408 a conservative uncertainty of $40 \text{ J m}^{-2} \text{ s}^{-0.5} \text{ K}^{-1}$, based on the shape of
 409 the χ^2 curve around the minima of the ‘no roughness’ and ‘low roughness’
 410 models (see Figure 3). The uncertainty on the p_V values are derived using
 411 the 10% relative error on D_V . Table 2 summarizes our results.

412

413 [Table 2 about here.]

414 5. Discussion

415 5.1. Size and albedo

416 The best-fit values of D_V obtained from our TPM analysis of MIDI data,
 417 247 ± 25 km and 238 ± 24 km, presents an offset of about 30 km with the nom-
 418 inal value (211 ± 21 km). Even though these values are in agreement within
 419 the error bars, our TPM results seem to favor a larger diameter for (16) Psy-
 420 che. We remind that the condition of convexity, imposed by the lightcurve
 421 inversion technique (see [Kaasalainen and Torppa 2001](#)), may introduce such
 422 a systematic bias on the size determination when large concavities are present
 423 on the asteroid surface. In this case, the volume-equivalent diameter obtained
 424 when using a convex shape will overestimate the ‘true’ volume and then the
 425 size of the asteroid. In our preceding analysis of (41) Daphne with MIDI

426 ([Matter et al. 2011](#)), we faced a similar situation. The volume-equivalent di-
427 ameter derived with a convex shape model was overestimated, and the use of
428 a more detailed shape model, including concavities ([Carry 2009](#)), solved this
429 discrepancy. Although the diameter values of 247 km and 238 km we derived
430 here are close to the average diameter of all reported estimates for Psyche
431 (247 ± 19 km, see [Carry 2012](#)), we expect the real value to be somehow smaller.

432

433 Using our TPM diameter estimation, we derived a geometric visible albedo
434 value in the range between 0.12 and 0.13. As expected from the IRAS and
435 AKARI size estimates, our estimate lies between the values derived from
436 those surveys, namely 0.120 ± 0.004 and 0.18 ± 0.01 , respectively. Those val-
437 ues are not identical within uncertainties. This discrepancy is probably due
438 to the fact that we are comparing our volume equivalent diameter estimate
439 with instantaneous area equivalent diameters measured at different epochs.
440 Nevertheless, those albedo values are in good agreement with the M-type
441 taxonomic type of (16) Psyche (by definition, M-types have an albedo be-
442 tween 0.075 and 0.30).

443

444 *5.2. Thermal properties*

445 As detailed in the introduction, infrared interferometry can spatially
446 probe the asteroid surface temperature distribution in different directions
447 at high angular resolution. Used in combination with infrared radiometry,
448 it can help to remove the degeneracy existing in our constraints of thermal
449 inertia and surface roughness and this at one single epoch, as already shown
450 in [Matter et al. \(2011\)](#).

451 We obtained good constraints on the determination of macroscopic rough-
452 ness of (16) Psyche. Both no- and low- roughness models appears equally
453 good in terms of our best-fit estimator. We estimate that the corresponding
454 mean surface slope, as defined by [Hapke \(1984\)](#), should be lower than 10° for
455 (16) Psyche. A high macroscopic roughness is discarded. We remind that the
456 roughness is at scales ranging from several centimeters to a fraction of the
457 length of a facet, the latter being of the order of 10 kilometer. Interestingly,
458 radar data reported by [Shepard et al. \(2008\)](#) give a very low polarization
459 ratio of 0.06 ± 0.02 for (16) Psyche, which indicates a smooth surface with-
460 out significant radar-wavelength-scale surface roughness. Nevertheless, this
461 agreement has to be considered with caution since the macroscopic surface
462 roughness probed by infrared interferometry may be at a scale different than
463 that constrained by radar observations.

464 In addition, our TPM analysis indicates that (16) Psyche has a thermal
465 inertia value lying between 114 ± 40 and $120 \pm 40 J m^{-2} s^{-0.5} K^{-1}$. This
466 is significantly larger than the thermal inertia values generally measured on
467 main-belt asteroids larger than 100 km in diameter (see [Figure 5](#)). Indeed,
468 large main-belt asteroids such as (1) Ceres, (2) Pallas, (3) Juno, (4) Vesta,
469 (21) Lutetia, (41) Daphne, (65) Cybele, or (532) Herculina present a very low
470 thermal inertia, between 5 and $30 J m^{-2} s^{-0.5} K^{-1}$ ([Mueller and Lagerros](#)
471 [1998](#); [Müller and Blommaert 2004](#); [Lamy et al. 2010](#); [Matter et al. 2011](#)).
472 [Mueller et al. \(2010\)](#) also measured a low thermal inertia of
473 $20 \pm 15 J m^{-2} s^{-0.5} K^{-1}$ for the large binary Trojan (617) Patroclus. More
474 recently, [Marchis et al. \(2012\)](#) also found thermal inertia potentially lower
475 than $100 J m^{-2} s^{-0.5} K^{-1}$ for 200 km-class main-belt asteroids, except

476 for the M-type asteroid (22) Kalliope, which could exhibit a higher value
477 ($\Gamma = 5 - 250 J m^{-2} s^{-0.5} K^{-1}$). One exception is the asteroid (694) Ekard
478 for which [Delbo and Tanga \(2009\)](#) determined a thermal inertia value around
479 100-140 $J m^{-2} s^{-0.5} K^{-1}$. However, the TPM fit to the IRAS data for this
480 asteroid was the worst among those studied in that work, indicating that the
481 thermal inertia value for (694) Ekard might be less accurate compared to the
482 other values derived for asteroids with sizes larger than 100 km. All those
483 measurements imply that the surfaces of those large bodies are likely covered
484 by a thick layer of fine-grained dust regolith. This is expected for such large
485 bodies that can gravitationally retain on their surface loose material like thin
486 dust produced from impact ejecta. On the other hand, smaller asteroids of
487 a few km or tens of km in size have lower gravity and are expected to retain
488 less regolith from impacts.

489 In general, existing measurements shows a decrease in the thermal inertia
490 value with increasing asteroid diameter (see e.g., [Delbo et al. 2007](#); [Delbo and Tanga](#)
491 [2009](#)). This suggests that the thermal inertia of asteroids is mainly controlled
492 by the dusty nature of the asteroid surface rather than other physical param-
493 eters associated to the nature of the material itself. This especially concerns
494 thermal conductivity as thermal inertia only varies as the square root of
495 the conductivity. Since (16) Psyche is a large main-belt asteroid, its surface
496 should be also covered by such a thick and thermally insulating dust regolith,
497 which would imply a low thermal inertia. Therefore, the high thermal in-
498 ertia value we measured strongly suggests a significant difference in terms
499 of composition, so that it would sufficiently increase the thermal conductiv-
500 ity of its surface and then its thermal inertia. This may also explain the

501 potentially high thermal inertia ($5\text{-}250 J m^{-2} s^{-0.5} K^{-1}$) measured for the
502 large M-type asteroid (22) Kalliope (Marchis et al. 2012). As stated in the
503 introduction, metal is an excellent thermal conductor, potentially leading to
504 an enhanced thermal inertia. In this context, Opeil et al. (2010) measured
505 the thermal conductivity of a sample of meteorites including two ordinary
506 chondrites, one enstatite chondrite, two carbonaceous chondrites and one
507 iron meteorite. They showed that the thermal conductivity, at low temper-
508 atures (5 to 300 K), of iron meteorites is much higher, by about one order
509 of magnitude, than the one of stony meteorites, especially the ordinary and
510 carbonaceous chondrites. Interestingly, one order of magnitude difference in
511 thermal conductivity corresponds to a factor 3 to 4 in thermal inertia, which
512 is roughly the discrepancy between our thermal inertia measurement for (16)
513 Psyche, around $120 J m^{-2} s^{-0.5} K^{-1}$, and the average thermal inertia of other
514 large main-belt asteroids, around $30 J m^{-2} s^{-0.5} K^{-1}$. As a consequence, a
515 metallic surface composition appears as a realistic explanation for the high
516 thermal inertia we measured on the surface of (16) Psyche. Our results thus
517 constitute a new evidence of the metal-rich composition of (16) Psyche, and
518 confirm the previous radar studies on this object (e.g., Shepard et al. 2010).

519

520 [Figure 5 about here.]

521 We show in Fig. 5 all the existing thermal inertia measurements of main-
522 belt asteroids larger than 100 km in diameter, including our measurement
523 for (16) Psyche. We can see that the two M-type asteroids of the list, (16)
524 Psyche and potentially (22) Kalliope, somehow sticks out from the thermal

525 inertia range of large MBAs. This difference is even noticeable with P-type
526 asteroids, which show thermal inertia values comparable to the one of C-
527 complex and S-complex asteroids. This is in agreement with the expectation
528 that P-type asteroids have surface materials rich in carbon and/or organics
529 (Vilas and Smith 1985; Hiroi et al. 2004), which are less thermally conduc-
530 tive. Figure 5 thus illustrates how the relation between size and thermal
531 inertia, highlighted for instance in Delbo and Tanga (2009), can be modi-
532 fied when asteroids with similar sizes but different compositions, especially
533 metallic, are considered.

534

535 6. Summary

536 We have obtained the first successful interferometric observations of the
537 M-type asteroid (16) Psyche using the MIDI instrument and the 16m-long
538 baseline E0-G0 of the VLTI.

539 Following the work of Matter et al. (2011), we applied our thermophysical
540 model (TPM) to the MIDI observations of (16) Psyche to derive its size
541 and the thermal properties of its surface. Using the convex shape model of
542 Kaasalainen et al. (2002), our TPM results indicate that Psyche has a vol-
543 ume equivalent diameter between 238 ± 24 and 247 ± 25 km, depending on
544 the assumed surface roughness.

545

546 Our analysis also showed that a low macroscopic surface roughness is
547 clearly favored by our interferometric observations, and that ‘high rough-
548 ness’ models are discarded. With such a constraint on the macroscopic

549 roughness, the TPM results indicate a high thermal inertia for (16) Psy-
550 che, of $130 J m^{-2} s^{-0.5} K^{-1}$ ('no roughness') or $114 J m^{-2} s^{-0.5} K^{-1}$ ('low
551 roughness'), with a total uncertainty estimated at $40 J m^{-2} s^{-0.5} K^{-1}$. This
552 is one of the highest thermal inertia ever measured for a 200 km-class aster-
553 oid. This is in clear contradiction with previous results indicating that the
554 surface of asteroids with sizes larger than 100 km have a low thermal iner-
555 tia. As metal is an excellent thermal conductor, we expect this high thermal
556 inertia to be another evidence of the metallic composition of (16) Psyche, as
557 previously inferred from radar studies. This reinforces the hypothesis of (16)
558 Psyche as originated from the fragmentation of the iron core of a differenti-
559 ated parent body or more likely, considering its size, from the collision and
560 aggregation of several objects, with at least one of them being purely metallic.

561

562 *Acknowledgments*

563 We would like to thank the referees for their comments and suggestions
564 that helped to improve significantly this manuscript. We would also like to
565 thank the staff and the Science Archive Operation of the European South-
566 ern Observatory (ESO) for their support in the acquisition of the data.
567 The development of the asteroid thermophysical model used in this work
568 was partially supported by the project 11-BS56-008 (Shocks) of the Agence
569 National de la Recherche (ANR). This research used the Miriade VO tool
570 ([Berthier et al. 2008](#)) developed at IMCCE.

571 **References**

572 Bell, J. F., Davis, D. R., Hartmann, W. K., Gaffey, M. J., 1989. Asteroids

573 - The big picture. In: Binzel, R. P., Gehrels, T., Matthews, M. S. (Eds.),
574 Asteroids II. pp. 921–945.

575 Berthier, J., Hestroffer, D., Carry, B., Durech, J., Tanga, P., Delbo, M.,
576 Vachier, F., 2008. A Service of Position and Physical Ephemerides Com-
577 putation Dedicated to the Small Bodies of the Solar System. LPI Contri-
578 butions 1405, 8374.

579 Bottke, W. F., Durda, D. D., Nesvorný, D., Jedicke, R., Morbidelli, A.,
580 Vokrouhlický, D., Levison, H. F., Dec. 2005. Linking the collisional his-
581 tory of the main asteroid belt to its dynamical excitation and depletion.
582 *Icarus*179, 63–94.

583 Bottke, W. F., Nesvorný, D., Grimm, R. E., Morbidelli, A., O’Brien, D. P.,
584 Feb. 2006. Iron meteorites as remnants of planetesimals formed in the
585 terrestrial planet region. *Nature*439, 821–824.

586 Bus, S. J., Binzel, R. P., Jul. 2002. Phase II of the Small Main-Belt Asteroid
587 Spectroscopic Survey A Feature-Based Taxonomy. *Icarus*158, 146–177.

588 Carry, B., 2009. Etude des propriétés physiques des astéroïdes par imagerie à
589 haute résolution angulaire. Ph.D. thesis, Université Paris 7- Observatoire
590 de Paris/LESIA.

591 Carry, B., Dec. 2012. Density of asteroids. *Plan. and Space Sci.*73, 98–118.

592 Cellino, A., Diolaiti, E., Ragazzoni, R., Hestroffer, D., Tanga, P., Ghedina,
593 A., Apr. 2003. Speckle interferometry observations of asteroids at tng*.
594 *Icarus*162, 278–284.

- 595 Chesneau, O., Oct. 2007. MIDI: Obtaining and analysing interferometric data
596 in the mid-infrared. *New Astron. Rev.*51, 666–681.
- 597 Cloutis, E. A., Gaffey, M. J., Smith, D. G. W., Lambert, R. S. J., Jun. 1990.
598 Metal Silicate Mixtures: Spectral Properties and Applications to Asteroid
599 Taxonomy. *J. Geophys. Res.*95, 8323–8338.
- 600 Cohen, M., Walker, R. G., Carter, B., Hammersley, P., Kidger, M., Noguchi,
601 K., Apr. 1999. Spectral Irradiance Calibration in the Infrared. X. A Self-
602 Consistent Radiometric All-Sky Network of Absolutely Calibrated Stellar
603 Spectra. *Astron. J.*117, 1864–1889.
- 604 Delbo, M., Dell’Oro, A., Harris, A. W., Mottola, S., Mueller, M., Sep. 2007.
605 Thermal inertia of near-Earth asteroids and implications for the magnitude
606 of the Yarkovsky effect. *Icarus*190, 236–249.
- 607 Delbo, M., Ligi, S., Matter, A., Cellino, A., Berthier, J., Apr. 2009. First
608 VLTI-MIDI Direct Determinations of Asteroid Sizes. *Astrophys. J.*694,
609 1228–1236.
- 610 Delbo, M., Tanga, P., Feb. 2009. Thermal inertia of main belt asteroids
611 smaller than 100 km from IRAS data. *Plan. and Space Sci.*57, 259–265.
- 612 DeMeo, F. E., Binzel, R. P., Slivan, S. M., Bus, S. J., Jul. 2009. An extension
613 of the Bus asteroid taxonomy into the near-infrared. *Icarus*202, 160–180.
- 614 Descamps, P., Marchis, F., Berthier, J., Emery, J. P., Duchêne, G., de Pater,
615 I., Wong, M. H., Lim, L., Hammel, H. B., Vachier, F., Wiggins, P., Teng-
616 Chuen-Yu, J.-P., Peyrot, A., Pollock, J., Assafin, M., Vieira-Martins, R.,

617 Camargo, J. I. B., Braga-Ribas, F., Macomber, B., Feb. 2011. Triplicity
618 and physical characteristics of Asteroid (216) Kleopatra. *Icarus*211, 1022–
619 1033.

620 Descamps, P., Marchis, F., Pollock, J., Berthier, J., Vachier, F., Birlan,
621 M., Kaasalainen, M., Harris, A. W., Wong, M. H., Romanishin, W. J.,
622 Cooper, E. M., Kettner, K. A., Wiggins, P., Kryszczyńska, A., Polinska,
623 M., Coliac, J.-F., Devyatkin, A., Verestchagina, I., Gorshanov, D., Aug.
624 2008. New determination of the size and bulk density of the binary Asteroid
625 22 Kalliope from observations of mutual eclipses. *Icarus*196, 578–600.

626 Drummond, J., Christou, J., Oct. 2008. Triaxial ellipsoid dimensions and
627 rotational poles of seven asteroids from Lick Observatory adaptive optics
628 images, and of Ceres. *Icarus*197, 480–496.

629 Drummond, J. D., Christou, J., Dec. 2006. Sizing up Asteroids at Lick Ob-
630 servatory with Adaptive Optics. In: AAS/Division for Planetary Sciences
631 Meeting Abstracts #38. Vol. 38 of Bulletin of the American Astronomical
632 Society. p. 1304.

633 Durech, J., Kaasalainen, M., Herald, D., Dunham, D., Timerson, B., Hanuš,
634 J., Frappa, E., Talbot, J., Hayamizu, T., Warner, B. D., Pilcher, F., Galád,
635 A., Aug. 2011. Combining asteroid models derived by lightcurve inversion
636 with asteroidal occultation silhouettes. *Icarus*214, 652–670.

637 Durech, J., Sidorin, V., Kaasalainen, M., Apr. 2010. DAMIT: a database of
638 asteroid models. *Astron. and Astrophys.*513, A46.

- 639 Emery, J. P., Cruikshank, D. P., van Cleve, J., Jun. 2006. Thermal emission
640 spectroscopy (5.2–38 μm) of three Trojan asteroids with the Spitzer Space
641 Telescope: Detection of fine-grained silicates. *Icarus*182, 496–512.
- 642 Fornasier, S., Clark, B. E., Dotto, E., Migliorini, A., Ockert-Bell, M., Barucci,
643 M. A., Dec. 2010. Spectroscopic survey of M-type asteroids. *Icarus*210,
644 655–673.
- 645 Hanus, J., Marchis, F., Durech, J., Oct. 2012. Asteroid Sizes Deter-
646 mined by Combining Shape Models and Keck Adaptive Optics Images.
647 In: AAS/Division for Planetary Sciences Meeting Abstracts. Vol. 44 of
648 AAS/Division for Planetary Sciences Meeting Abstracts. p. 302.08.
- 649 Hapke, B., Jul. 1984. Bidirectional reflectance spectroscopy. III - Correction
650 for macroscopic roughness. *Icarus*59, 41–59.
- 651 Hardersen, P. S., Gaffey, M. J., Abell, P. A., May 2005. Near-IR spectral
652 evidence for the presence of iron-poor orthopyroxenes on the surfaces of
653 six M-type asteroids. *Icarus*175, 141–158.
- 654 Hiroi, T., Pieters, C. M., Rutherford, M. J., Zolensky, M. E., Sasaki, S.,
655 Ueda, Y., Miyamoto, M., Mar. 2004. What are the P-type Asteroids Made
656 Of? In: Mackwell, S., Stansbery, E. (Eds.), Lunar and Planetary Insti-
657 tute Science Conference Abstracts. Vol. 35 of Lunar and Planetary Inst.
658 Technical Report. p. 1616.
- 659 Jaffe, W. J., Oct. 2004. Coherent fringe tracking and visibility estimation for
660 MIDI. In: Traub, W. A. (Ed.), Society of Photo-Optical Instrumentation

661 Engineers (SPIE) Conference Series. Vol. 5491 of Society of Photo-Optical
662 Instrumentation Engineers (SPIE) Conference Series. p. 715.

663 Jakosky, B. M., Apr. 1986. On the thermal properties of Martian fines.
664 *Icarus*66, 117–124.

665 Jakosky, B. M., Finiol, G. W., Henderson, B. G., Jun. 1990. Directional vari-
666 ations in thermal emission from geologic surfaces. *Geophys. Res. Lett.*17,
667 985–988.

668 Kaasalainen, M., Torppa, J., Sep. 2001. Optimization Methods for Asteroid
669 Lightcurve Inversion. I. Shape Determination. *Icarus*153, 24–36.

670 Kaasalainen, M., Torppa, J., Piironen, J., Oct. 2002. Models of Twenty As-
671 teroids from Photometric Data. *Icarus*159, 369–395.

672 Kuzmanoski, M., Kovačević, A., Nov. 2002. Motion of the asteroid (13206)
673 1997GC22 and the mass of (16) Psyche. *Astron. and Astrophys.*395, L17–
674 L19.

675 Lamy, P. L., Groussin, O., Fornasier, S., Jorda, L., Kaasalainen, M., Barucci,
676 M. A., Jun. 2010. Thermal properties of asteroid 21 Lutetia from Spitzer
677 Space Telescope observations. *Astron. and Astrophys.*516, A74.

678 Lebofsky, L. A., Sykes, M. V., Tedesco, E. F., Veeder, G. J., Matson, D. L.,
679 Brown, R. H., Gradie, J. C., Feierberg, M. A., Rudy, R. J., Nov. 1986. A
680 refined 'standard' thermal model for asteroids based on observations of 1
681 Ceres and 2 Pallas. *Icarus*68, 239–251.

682 Leinert, C., van Boekel, R., Waters, L. B. F. M., Chesneau, O., Malbet, F.,
683 Köhler, R., Jaffe, W., Ratzka, T., Dutrey, A., Preibisch, T., Graser, U.,
684 Bakker, E., Chagnon, G., Cotton, W. D., Dominik, C., Dullemond, C. P.,
685 Glazenberg-Kluttig, A. W., Glindemann, A., Henning, T., Hofmann, K.-
686 H., de Jong, J., Lenzen, R., Ligi, S., Lopez, B., Meisner, J., Morel, S.,
687 Paresce, F., Pel, J.-W., Percheron, I., Perrin, G., Przygodda, F., Richichi,
688 A., Schöller, M., Schuller, P., Stecklum, B., van den Ancker, M. E., von der
689 Lühe, O., Weigelt, G., Aug. 2004. Mid-infrared sizes of circumstellar disks
690 around Herbig Ae/Be stars measured with MIDI on the VLTI. *Astron. and*
691 *Astrophys.*423, 537–548.

692 Leyrat, C., Barucci, A., Mueller, T., O’Rourke, L., Valtchanov, I., Fornasier,
693 S., Mar. 2012. Thermal properties of (4) Vesta derived from Herschel mea-
694 surements. *Astron. and Astrophys.*539, A154.

695 Lupishko, D. F., May 2006. On the bulk density of the M-type asteroid 16
696 Psyche. *Solar System Research* 40, 214–218.

697 Marchis, F., Enriquez, J. E., Emery, J. P., Mueller, M., Baek, M., Pollock,
698 J., Assafin, M., Vieira Martins, R., Berthier, J., Vachier, F., Cruikshank,
699 D. P., Lim, L. F., Reichart, D. E., Ivarsen, K. M., Haislip, J. B., LaCluyze,
700 A. P., Nov. 2012. Multiple asteroid systems: Dimensions and thermal
701 properties from Spitzer Space Telescope and ground-based observations.
702 *Icarus*221, 1130–1161.

703 Matter, A., Delbo, M., Ligi, S., Crouzet, N., Tanga, P., Sep. 2011. Deter-
704 mination of physical properties of the Asteroid (41) Daphne from interfer-
705 ometric observations in the thermal infrared. *Icarus*215, 47–56.

- 706 Mueller, M., 2007. Surface properties of asteroids from mid-infrared observa-
707 tions and thermophysical modeling. Ph.D. thesis, Freie Universitaet Berlin.
- 708 Mueller, M., Marchis, F., Emery, J. P., Harris, A. W., Mottola, S., Hestrof-
709 fer, D., Berthier, J., di Martino, M., Feb. 2010. Eclipsing binary Trojan
710 asteroid Patroclus: Thermal inertia from Spitzer observations. *Icarus*205,
711 505–515.
- 712 Mueller, T. G., Lagerros, J. S. V., Oct. 1998. Asteroids as far-infrared pho-
713 tometric standards for ISOPHOT. *Astron. and Astrophys.*338, 340–352.
- 714 Müller, T. G., Blommaert, J. A. D. L., Apr. 2004. 65 Cybele in the thermal
715 infrared: Multiple observations and thermophysical analysis. *Astron. and*
716 *Astrophys.*418, 347–356.
- 717 Opeil, C. P., Consolmagno, G. J., Britt, D. T., Jul. 2010. The thermal con-
718 ductivity of meteorites: New measurements and analysis. *Icarus*208, 449–
719 454.
- 720 O’Rourke, L., Müller, T., Valtchanov, I., Altieri, B., González-Garcia, B. M.,
721 Bhattacharya, B., Jorda, L., Carry, B., Küppers, M., Groussin, O., Al-
722 twegg, K., Barucci, M. A., Bockelee-Morvan, D., Crovisier, J., Dotto, E.,
723 Garcia-Lario, P., Kidger, M., Llorente, A., Lorente, R., Marston, A. P.,
724 Sanchez Portal, M., Schulz, R., Sierra, M., Teyssier, D., Vavrek, R., Jun.
725 2012. Thermal and shape properties of asteroid (21) Lutetia from Herschel
726 observations around the Rosetta flyby. *Plan. and Space Sci.*66, 192–199.
- 727 Ostro, S. J., Campbell, D. B., Shapiro, I. I., Aug. 1985. Mainbelt asteroids -
728 Dual-polarization radar observations. *Science* 229, 442–446.

- 729 Perrin, G., Leinert, C., Graser, U., Waters, L. B. F. M., Lopez, B., 2003.
730 MIDI, the 10 μm interferometer of the VLT. In: G. Perrin & F. Malbet
731 (Ed.), EAS Publications Series. Vol. 6. p. 127.
- 732 Pravec, P., Harris, A. W., Kušnirák, P., Galád, A., Hornoch, K., Sep. 2012.
733 Absolute magnitudes of asteroids and a revision of asteroid albedo esti-
734 mates from WISE thermal observations. *Icarus*221, 365–387.
- 735 Rivkin, A. S., Howell, E. S., Britt, D. T., Lebofsky, L. A., Nolan, M. C.,
736 Branston, D. D., Sep. 1995. Three-micron spectrometric survey of M-and
737 E-class asteroids. *Icarus*117, 90–100.
- 738 Rivkin, A. S., Howell, E. S., Lebofsky, L. A., Clark, B. E., Britt, D. T.,
739 Jun. 2000. The nature of M-class asteroids from 3-micron observations.
740 *Icarus*145, 351–368.
- 741 Shepard, M. K., Clark, B. E., Nolan, M. C., Howell, E. S., Magri, C., Giorgini,
742 J. D., Benner, L. A. M., Ostro, S. J., Harris, A. W., Warner, B., Pray, D.,
743 Pravec, P., Fauerbach, M., Bennett, T., Klotz, A., Behrend, R., Correia,
744 H., Coloma, J., Casulli, S., Rivkin, A., May 2008. A radar survey of M-
745 and X-class asteroids. *Icarus*195, 184–205.
- 746 Shepard, M. K., Clark, B. E., Ockert-Bell, M., Nolan, M. C., Howell, E. S.,
747 Magri, C., Giorgini, J. D., Benner, L. A. M., Ostro, S. J., Harris, A. W.,
748 Warner, B. D., Stephens, R. D., Mueller, M., Jul. 2010. A radar survey of
749 M- and X-class asteroids II. Summary and synthesis. *Icarus*208, 221–237.
- 750 Sih, S. S., Barlow, J. W., 2004. The prediction of the emissivity and thermal

751 conductivity of powder beds. *Particulate Science and Technology* 22 (4),
752 427–440.

753 Tedesco, E. F., Noah, P. V., Noah, M., Price, S. D., Feb. 2002. The Supple-
754 mental IRAS Minor Planet Survey. *Astron. J.*123, 1056–1085.

755 Tholen, D. J., 1984. Asteroid taxonomy from cluster analysis of Photometry.
756 Ph.D. thesis, Arizona Univ., Tucson.

757 Usui, F., Kuroda, D., Müller, T. G., Hasegawa, S., Ishiguro, M., Ootsubo,
758 T., Ishihara, D., Kataza, H., Takita, S., Oyabu, S., Ueno, M., Matsuhara,
759 H., Onaka, T., Oct. 2011. Asteroid Catalog Using Akari: AKARI/IRC
760 Mid-Infrared Asteroid Survey. *PUBL ASTRON SOC JAP*63, 1117–1138.

761 Verhoelst, T., May 2005. Evolved stars: a combined view vrom interferom-
762 etry and spectroscopy. Ph.D. thesis, Institute of Astronomy, K.U.Leuven,
763 Belgium.

764 Veverka, J., Farquhar, B., Robinson, M., Thomas, P., Murchie, S., Harch, A.,
765 Antreasian, P. G., Chesley, S. R., Miller, J. K., Owen, W. M., Williams,
766 B. G., Yeomans, D., Dunham, D., Heyler, G., Holdridge, M., Nelson,
767 R. L., Whittenburg, K. E., Ray, J. C., Carcich, B., Cheng, A., Chapman,
768 C., Bell, J. F., Bell, M., Bussey, B., Clark, B., Domingue, D., Gaffey,
769 M. J., Hawkins, E., Izenberg, N., Joseph, J., Kirk, R., Lucey, P., Malin,
770 M., McFadden, L., Merline, W. J., Peterson, C., Prockter, L., Warren, J.,
771 Wellnitz, D., Sep. 2001a. The landing of the NEAR-Shoemaker spacecraft
772 on asteroid 433 Eros. *Nature*413, 390–393.

773 Veverka, J., Thomas, P. C., Robinson, M., Murchie, S., Chapman, C., Bell,
774 M., Harch, A., Merline, W. J., Bell, J. F., Bussey, B., Carcich, B., Cheng,
775 A., Clark, B., Domingue, D., Dunham, D., Farquhar, R., Gaffey, M. J.,
776 Hawkins, E., Izenberg, N., Joseph, J., Kirk, R., Li, H., Lucey, P., Malin,
777 M., McFadden, L., Miller, J. K., Owen, W. M., Peterson, C., Prockter, L.,
778 Warren, J., Wellnitz, D., Williams, B. G., Yeomans, D. K., Apr. 2001b.
779 Imaging of Small-Scale Features on 433 Eros from NEAR: Evidence for a
780 Complex Regolith. *Science* 292, 484–488.

781 Viateau, B., Feb. 2000. Mass and density of asteroids (16) Psyche and (121)
782 Hermione. *Astron. and Astrophys.*354, 725–731.

783 Vilas, F., Smith, B. A., Dec. 1985. Reflectance spectrophotometry (about
784 0.5-1.0 micron) of outer-belt asteroids - Implications for primitive, organic
785 solar system material. *Icarus*64, 503–516.

786 Yano, H., Kubota, T., Miyamoto, H., Okada, T., Scheeres, D., Takagi, Y.,
787 Yoshida, K., Abe, M., Abe, S., Barnouin-Jha, O., Fujiwara, A., Hasegawa,
788 S., Hashimoto, T., Ishiguro, M., Kato, M., Kawaguchi, J., Mukai, T.,
789 Saito, J., Sasaki, S., Yoshikawa, M., Jun. 2006. Touchdown of the Hayabusa
790 Spacecraft at the Muses Sea on Itokawa. *Science* 312, 1350–1353.

791 **List of Figures**

792	1	Observations	38
793	2	Predicted orientation of Psyche	39
794	3	Thermal inertia determination	40
795	4	Ratio photometry/model	41
796	5	Thermal inertia vs asteroid diameter	42

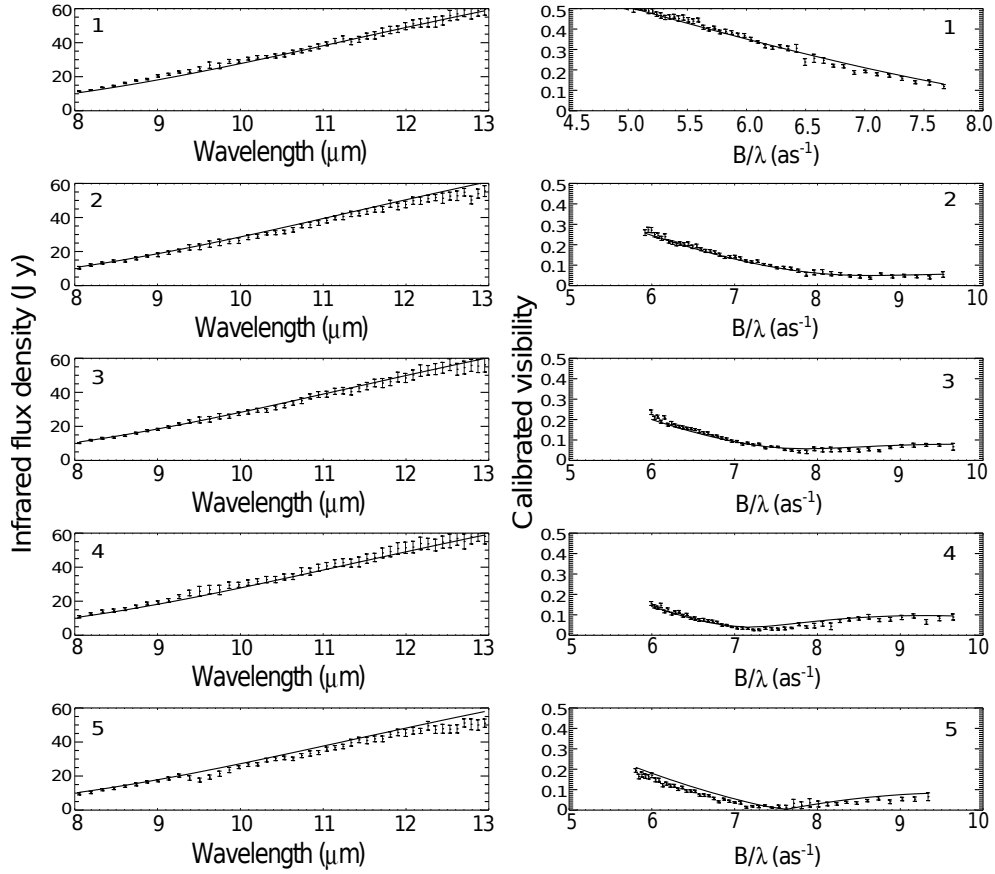


Figure 1: **Left panels:** measured thermal infrared fluxes (with error bars) and best-fit TPM infrared fluxes (solid lines) of (16) Psyche, plotted between 8 and 13 μm . **Right panels:** measured mid-infrared interferometric visibilities (with error bars) and best-fit TPM visibilities (solid lines) of (16) Psyche, plotted as a function of angular frequency. The best-fit model represented here is : ‘low roughness’, $\Gamma = 115 \text{ J m}^{-2} \text{ s}^{-0.5} \text{ K}^{-1}$. For each pair of flux and visibility measurements, we indicated the label (‘1’, ‘2’, ‘3’, ‘4’, ‘5’) of the corresponding observing epoch, as defined in Table 1.

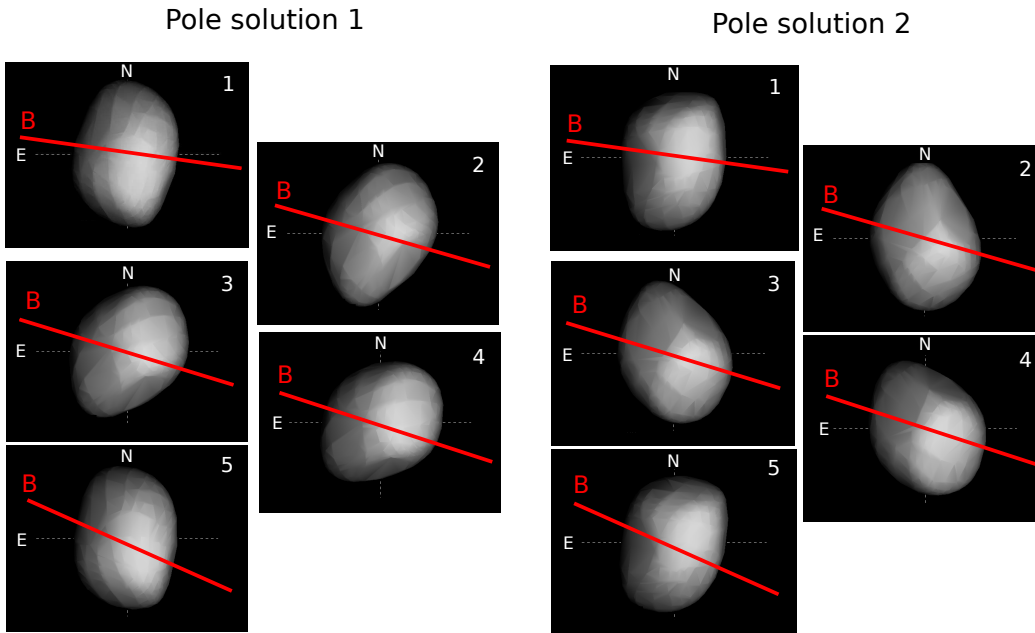


Figure 2: Representation of the expected orientation of (16) Psyche along with the projected baseline orientation at the time of the VLTI observations, on the plane of the sky; the North (N) and East (E) directions are indicated. We used the convex mesh and the two existing pole solutions derived by [Kaasalainen et al. \(2002\)](#) and detailed in Section 3. For each epoch, we indicated the corresponding label (1 to 5), as defined in Table 1.

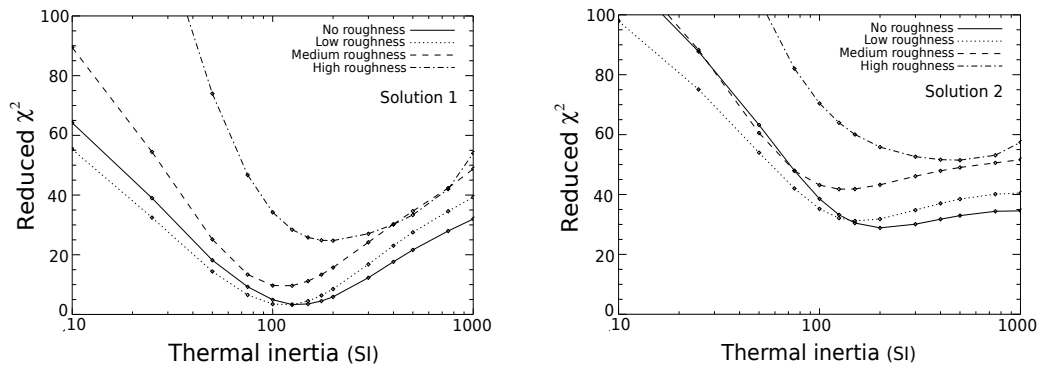


Figure 3: **Left:** plot of the reduced χ^2 , calculated from the TPM in the case of the first pole solution, as a function of thermal inertia Γ , for the four roughness models (see Section 3). **Right:** reduced χ^2 , calculated from the TPM in the case of the second pole solution.

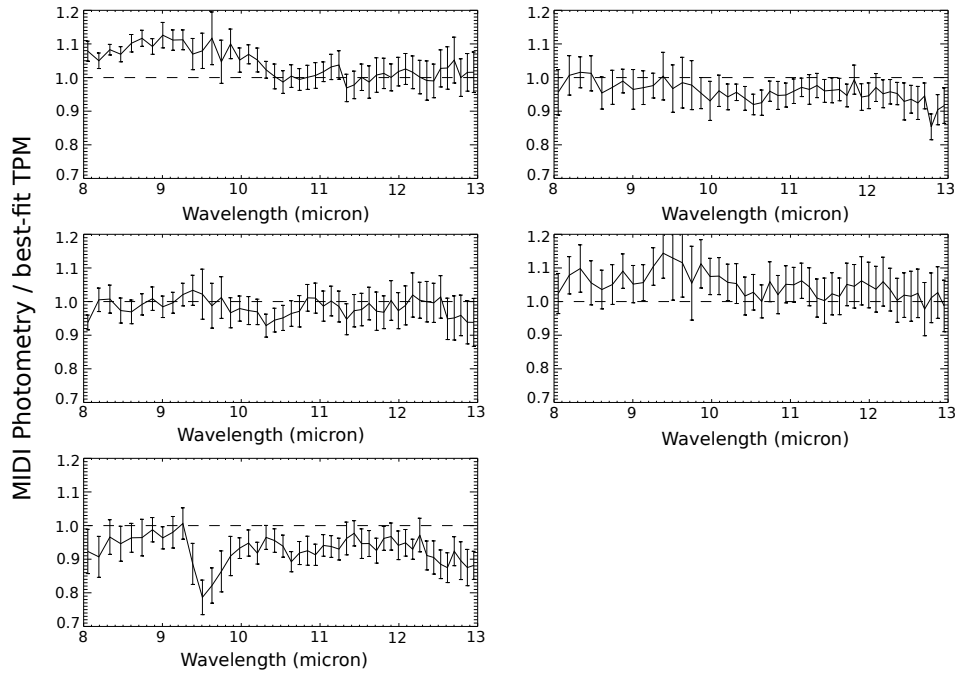


Figure 4: Ratio of the MIDI flux over the best-fit TPM shown in Figure 1, namely ‘low roughness’ and $\Gamma = 115 J m^{-2} s^{-0.5} K^{-1}$. We indicated the label corresponding to each observing epoch (‘1’ to ‘5’). Since we assumed an emissivity of 0.9 in our TPM, the level of the continuum (dashed line) is at 1.

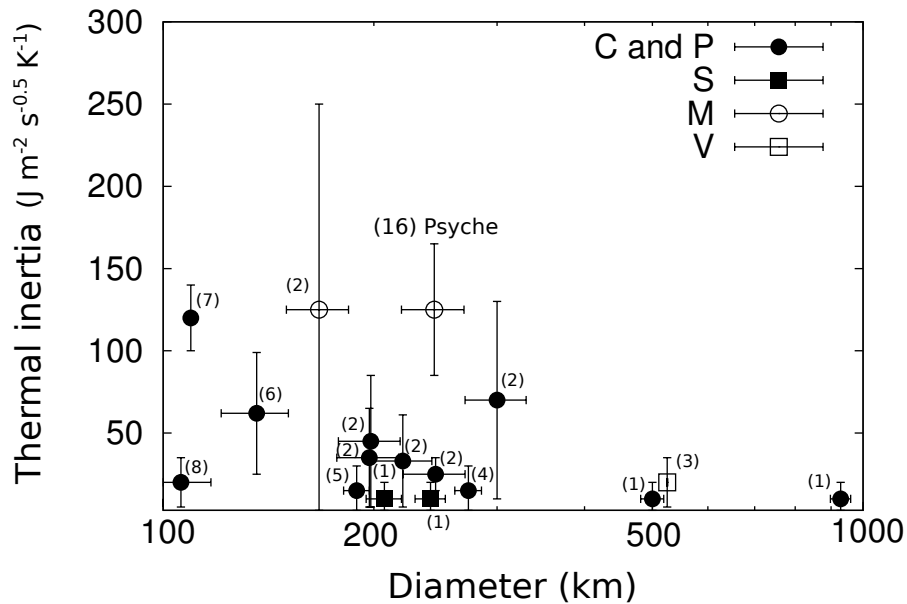


Figure 5: Compilation of the existing thermal inertia measurements of main-belt asteroids larger than 100 km in diameter. We included our new measurement for (16) Psyche. We indicated the taxonomic type (C-complex, S-complex and V-type) of each asteroid following [Bus and Binzel \(2002\)](#); [DeMeo et al. \(2009\)](#). We separated the X-complex into M-type and P-type asteroids, following the Tholen classification, to emphasize the higher thermal inertia of M-type asteroids. We also mention the corresponding references for each measurement: (1) [Mueller and Lagerros \(1998\)](#), (2) [Marchis et al. \(2012\)](#), (3) [Leyrat et al. \(2012\)](#), (4) [Müller and Blommaert \(2004\)](#), (5) [Matter et al. \(2011\)](#), (6) [Mueller et al. \(2010\)](#), (7) [Delbo and Tanga \(2009\)](#), (8) [O'Rourke et al. \(2012\)](#).

797 **List of Tables**

798	1	Observation log	44
799	2	Thermal properties	45

Object	Date (UT)	PBL (m)	PBLA ($^{\circ}$)	seeing ($''$)	airmass	Label
HD 29139	2010-12-30 00:24	11.3	82.0	1.50	1.70	Calib
(16) Psyche	2010-12-30 00:48	11.88	82.7	1.15	1.60	1
HD 29139	2010-12-30 02:59	14.4	79.0	1.00	1.40	Calib
(16) Psyche	2010-12-30 03:18	15.8	74.1	0.70	1.37	2
(16) Psyche	2010-12-30 03:30	16.0	73.3	0.75	1.37	3
(16) Psyche	2010-12-30 03:40	16.0	72.6	0.70	1.39	4
HD 29139	2010-12-30 03:58	15.9	70.5	0.60	1.40	Calib
HD 29139	2010-12-30 04:33	15.6	67.5	0.64	1.50	Calib
(16) Psyche	2010-12-30 04:51	15.5	66.5	0.75	1.60	5

Table 1: Log of the observations for (16) Psyche and its calibrator HD 29139, both observed with two ATs in E0-G0 configuration. PBL and PBLA stand for Projected BaseLine, and Projected BaseLine Angle, respectively. The last column gives a label for each interferometric observation of (16) Psyche, the label ‘Calib’ indicating a calibrator observation.

Roughness model	Reduced χ^2	Γ ($J m^{-2} s^{-0.5} K^{-1}$)	D_V (km)	p_V
No roughness	3.3	133 ± 40	247 ± 25	0.12 ± 0.02
Low roughness	3.2	114 ± 40	238 ± 24	0.13 ± 0.03

Table 2: Results of the determination of physical properties of the asteroid (16) Psyche, using the TPM. Γ is the thermal inertia, D_V is the spherical volume equivalent diameter, and p_V is the geometric visible albedo. The errors represent an estimation of the dominant contribution of the model systematics, as explained in Section 4.